#### **MATERIALS SCIENCE**

# Atomic-scale observation of dynamic grain boundary structural transformation during shear-mediated migration

Zhengwu Fang<sup>1</sup>†, Jianwei Xiao<sup>2</sup>†, Susheng Tan<sup>3</sup>, Chuang Deng<sup>2</sup>\*, Guofeng Wang<sup>1</sup>\*, Scott X. Mao<sup>1</sup>\*

Grain boundary (GB) structural change is commonly observed during and after stress-driven GB migration in nanocrystalline materials, but its exact atomic scale transformation has not been explored experimentally. Here, using in situ high-resolution transmission electron microscopy combined with molecular dynamics simulations, we observed the dynamic GB structural transformation stemming from reversible facet transformation and GB dissociation during the shear-mediated migration of faceted GBs in gold nanocrystals. A reversible transformation was found to occur between (002)/(111) and  $\Sigma$ 11(113) GB facets, accomplished by the coalescence and detachment of ( $\overline{11}$ 1)/(002)-type GB steps or disconnections that mediated the GB migration. In comparison, the dissociation of (002)/(111) GB into  $\Sigma$ 11(113) and  $\Sigma$ 3(111) GBs occurred via the reaction of (111)/(11 $\overline{1}$ )-type steps that involved the emission of partial dislocations. Furthermore, these transformations were loading dependent and could be accommodated by GB junctions. This work provides atomistic insights into the dynamic structural transformation during GB migration.

Copyright © 2022
The Authors, some rights reserved; exclusive licensee
American Association for the Advancement of Science. No claim to original U.S. Government Works. Distributed under a Creative
Commons Attribution
NonCommercial
License 4.0 (CC BY-NC).

#### **INTRODUCTION**

Grain boundary (GB), as the ubiquitous interfacial structure in polycrystalline materials, influences greatly the properties and microstructural development of materials (1). Grain growth and GB network evolution during plastic deformation in nanocrystalline materials have been widely reported (2-5), wherein stress-driven GB migration is regarded as a major phenomenon (6). Theoretical models, such as the dislocation glide mechanism for low-angle GBs (7, 8), the local conservative shuffling of atoms for high-angle GBs (9), and the unified disconnection-mediated mechanism (10, 11), have been proposed to describe the GB migration. However, these models do not consider the change of GB structure during and after the migration, which frequently happens in one of the most common GBs in polycrystalline materials, i.e., the asymmetrical tilt GBs (ATGBs) (12), especially in the GB with facets, and could affect their migration behaviors. For instance,  $\Sigma 11$  ATGBs (13) in Cu were found to show unique anisotropic mobility, which is associated with the transformation events at the facet nodes and incommensurate GB facets during the migration (14). Although the shear coupling factor of ATGBs might be predicted on the basis of the disconnection (10) or geometrical model (15, 16), there has been no direct experimental observation on the migration process or possible structural change at the atomic scale yet (3, 10, 17–20).

The faceted morphology is a typical feature of ATGBs (12, 21), which are formed via GB facet transformation (also termed as GB faceting). Broadly speaking, GB faceting, dissociation, and structural phase transformation all belong to GB complexion transition, as they involve the change of GB structure units (22). Previous studies

have indicated that GB complex transition could affect GB migration. For example, GB faceting can notably influence the thermally induced ATGB migration (23, 24), GB structural phase transformation can facilitate GB migration (25) or even alter the nature of GB migration (26), and the nonplanar GB structure formed by GB dissociation shows unique mechanical responses (27, 28). Nevertheless, the experimental evidence on the dynamic GB structural transformation during shear-mediated migration is still lacking. Moreover, a recent work revealed the absence of a correlation between GB velocity and curvature but a strong correlation between GB velocity and GB crystallography (e.g., misorientation and inclination) in Ni polycrystals (29), which further highlights the importance of investigating GB structural transformation during the migration and its impact on the kinetics of GB migration. With the help of the recently developed in situ transmission electron microscopy (TEM) platform (30), GB processing with controlled features and direct observation of the atomistic migration process under shear stress becomes attainable, which offers a great opportunity to explore this open area.

Here, in situ interface processing with controlled crystal orientation and in situ high-resolution TEM (HRTEM) shear testing were performed to study the ATGBs' migration behavior in gold (Au) nanobicrystals. Two kinds of faceted ATGBs, which consist of (002)/(111) ATGB facets and  $(\overline{11}1)/(002)$  or near  $(111)/(11\overline{1})$  nanofacets, were fabricated and studied. At equilibrium, (002)/(111) ATGB is a  $[1\overline{1}0]$  tilt incommensurate GB with a misorientation angle of 54.74°, which is found to coexist with  $\Sigma 11(113)$  symmetrical tilt GB (STGB) (with a misorientation angle of  $50.48^{\circ}$ ) (31) or (111)/(11 $\overline{1}$ ) GB (with a misorientation angle of 70.5°) (31, 32) and to be a common facet of  $\Sigma$ 11 ATGB in face-centered cubic (FCC) metals (33). A back-and-forth GB plane reorientation was observed during the migration process of the GB consisting of (002)/(111) and  $(\overline{111})/(002)$  facets, which is attributed to the reversible facet transformation between the (002)/ (111) and  $(\overline{11}1)/(002)$  ATGBs and the  $\Sigma 11(113)$  STGB. Moreover, the dissociation of GB into a  $\Sigma 11(113)$  STGB and a  $\Sigma 3(111)$  STGB was found during the migration of the GB consisting of (002)/(111) and

<sup>&</sup>lt;sup>1</sup>Department of Mechanical Engineering and Materials Science, University of Pittsburgh, Pittsburgh, PA 15261, USA. <sup>2</sup>Department of Mechanical Engineering, University of Manitoba, Winnipeg, MB R3Y1S1, Canada. <sup>3</sup>Petersen Institute of Nanoscience and Engineering, University of Pittsburgh, Pittsburgh, PA 15260, USA.

<sup>\*</sup>Corresponding author. Email: sxm2@pitt.edu (S.X.M.); guw8@pitt.edu (G.W.); chuang. deng@umanitoba.ca (C.D.)

<sup>†</sup>These authors contributed equally to this work.

near (111)/(11 $\overline{1}$ ) facets. The underlying atomistic mechanisms of these transformations were revealed with the atomistic molecular dynamics (MD) simulations. This work enriches our understanding of the atomistic migration mechanisms of high-angle ATGBs and offers direct evidence that dynamic GB structural transformation accommodates the stress-induced microstructural evolution in polycrystalline materials.

#### **RESULTS**

## Back-and-forth GB plane reorientation during shear-mediated migration

As shown in Fig. 1A, a [110] tilt Au bicrystal nanojunction with a diameter of ~10 nm and a misorientation angle of ~53.5° was fabricated by in situ nanowelding inside a TEM. The as-fabricated GB is a faceted GB that consists of the (002)<sub>1</sub>/(111)<sub>2</sub> ATGB facets and several interfacial defects connecting them (see section S1 and fig. S1 for the identification of GB positions and structure unit analysis). Here, we use "steps," instead of "disconnections," to denote these interfacial defects to distinguish them from the disconnections of  $\Sigma 11(113)$ STGB. The average GB plane has an inclination angle of ~11° to the (002)<sub>1</sub>/(111)<sub>2</sub> ATGB (see section S2 and fig. S2 for the definition and measurement of average inclination angle). A closer observation on the core structure of these steps shows that they all have a height of one  $(002)_1/(111)_2$  lattice spacing with  $(\overline{11}1)_1$  and  $(002)_2$ planes as abutting planes (Fig. 1I). Thereafter, these steps can be regarded as  $(\overline{11}1)_1/(002)_2$  nanofacets to some extent. Note that these nanofacets accommodate the deviation of the misorientation angle of this bicrystal from the ideal value of (002)/(111) ATGB (i.e., 54.74°), the inclination of the overall GB plane from the (002)<sub>1</sub>/(111)<sub>2</sub> ATGB, and the lattice misfit between (002)<sub>1</sub> and (111)<sub>2</sub> planes (34). Similar structural features have also been observed in a  $\Sigma 9$  {221} tilt GB in copper, where ATGB facets are connected by steps or STGB facets (35). A shear loading was then applied to the bottom grain of the bicrystal (denoted as G2 in Fig. 1A) at a constant rate (~0.001 nm s<sup>-1</sup>), and the loading direction (indicated by the white arrow in Fig. 1A) was nearly parallel to the  $(002)_1/(111)_2$  ATGB.

Under shear loading, some of the preexisting steps began to move leftward along the [112] direction of the bottom grain G2, causing the migration of the ATGB facets toward grain G2 (Fig. 1B). The migration behavior observed so far is similar to that of the conventional disconnection-mediated GB migration reported in other studies (10, 30), except that a new GB facet, which is identified as a  $\Sigma$ 11(113) STGB (36, 37), was formed at the right end of the GB in Fig. 1B. The zoom-in view of the STGB facet and the superimposed schematic in Fig. 1I confirm that the lattices at the two sides of this facet are in a symmetrical relation to the (113) plane. Note that the serrated GB structure consisting of (002)/(111) ATGB and  $\Sigma$ 11(113) STGB facets has been observed in Au polycrystals before (38). A slight clockwise rotation of the GB plane was found during this process, causing an increase in the average GB inclination angle (~5°). In the subsequent deformation, facet transformation and a back-and-forth GB plane reorientation were observed (Fig. 1, C to H, and movie S1). Note that a dislocation slip event happened within G1 between Fig. 1E and Fig. 1F, the details of which are shown in section S3 and fig. S3. To quantify the GB plane reorientation and establish the relationship between the facet transformation and the back-and-forth GB plane reorientation, the average GB inclination angle and the normalized facet ratio are plotted as a function of time in Fig. 1K (see fig. S2 and section S2 for the calculation of facet length ratio). The

change in the average inclination angle followed a "zig-zag" pattern with a minimum value of ~11° at the as-fabricated state and a maximum value of ~26°, which is close to the theoretical angle between (002) and (113) planes (i.e., 25.24°). The variation trend of the facet length ratio of  $\Sigma 11(113)$  STGB is similar to that of the average inclination angle, while the (002)<sub>1</sub>/(111)<sub>2</sub> ATGB and the steps exhibit the opposite trend (Fig. 1K). This relation is further confirmed by the plot of normalized facet length ratio versus inclination angle (Fig. 1L). Specifically, the increase in the average inclination angle is associated with the ATGB-to-STGB facet transformation and subsequent STGB facet migration at the expense of ATGB facets (Fig. 1, B to D, E and F, and G and H). On the basis of the energy pathway predicted from MD simulations as shown in fig. S4, the system energy is found to decrease with increasing inclination. In contrast, the decrease in the average inclination angle is related to the backward facet transformation at either side of the GB (Fig. 1, D and E, and F and G) and increases the system energy. The migration of the STGB facet is believed to follow the manner of nucleation and lateral motion of disconnections (30). Moreover, two different dynamic processes were captured at the facet junctions of the ATGB and the STGB: One is that a one-layer ATGB step  $[(\overline{111})_1/(002)_2 \text{ nanofacet}]$ was emitted from the facet node, causing the migration of the ATGB but keeping the STGB stationary (fig. S5, A and B); the other is that the ATGB kept immobile, but the STGB migrated several atomic layers (fig. S5, B to D). These processes are further validated by our MD simulation (fig. S5, E to H) and are attributed to the rearrangement of the localized atoms at the facet junctions. A slight grain rotation inevitably occurred during the shear loading, causing the misorientation angle of this bicrystal to gradually decrease to ~52° in Fig. 1G (see also fig. S6, A to D), which has accommodated the GB structural transformation during its migration (Fig. 1, A to H).

### Reversible facet transformation between the ATGB and the STGB

As shown in Fig. 1, the facet transformation between the (002)<sub>1</sub>/  $(111)_2$  ATGB and the  $\Sigma 11(113)$  STGB during the GB migration process was all accompanied by the annihilation or reappearance of  $(\overline{111})_1/(002)_2$  steps connecting the ATGB facets. Therefore, it is believed that these GB steps are highly involved in these processes. To verify this conjecture, a more detailed analysis of the atomistic deformation snapshots just before and after the formation of the STGB was conducted to explore the atomistic mechanism of ATGBto-STGB transformation (Fig. 2, A to D). As shown in Fig. 2 (A to C), a  $(\overline{111})_1/(002)_2$  step was found to nucleate and laterally move along the GB until it met another step, causing the migration of ATGB toward the bottom grain. Afterward, those steps disappeared and were replaced by a fully  $\Sigma 11(113)$  STGB at the same area, where the lattices at both sides of the GB were in symmetrical relation about (113) plane (Fig. 2D). Figure 2I shows the intensity profiles extracted along the blue solid lines in Fig. 2 (A to D). The rightward shift of peaks in those intensity profiles indicates an increase in lattice spacing between the atom columns (numbered from 0 to 6) arising from the motion of the step. Tracking the change of spacing from columns 0 to 4 (denoted as 01, 12, 23, and 34), we found that the lattice spacing of 01 and 12 fluctuated around 2.5 Å (Fig. 2J), which is the ideal value for  $\left|\frac{1}{4}\langle 112\rangle\right|$  in Au. In contrast, the lattice spacing of 23 and 34 increased from ~2.5 to ~2.88 Å (Fig. 2J); the latter is the ideal value for  $\left|\frac{1}{2}\langle 110\rangle\right|$  in Au. This change of lattice spacing further confirms the  $(\tilde{1}11)_2$ -to- $(002)_1$  plane transformation that resulted from

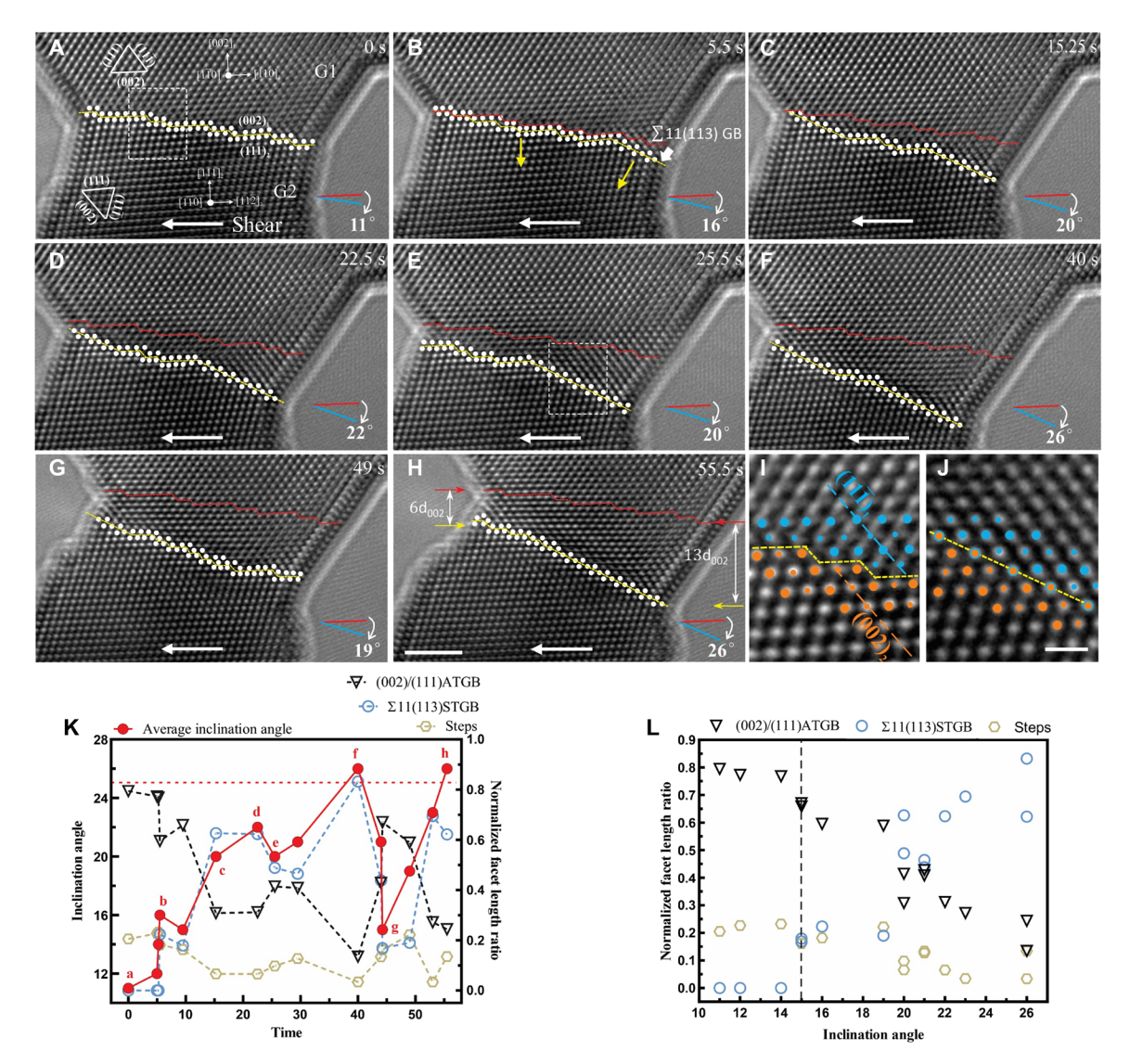


**Fig. 1. Stress-driven migration of a faceted GB accompanied by back-and-forth GB plane reorientation and reversible facet transformation.** (**A**) Structure of an as-fabricated Au bicrystal with a faceted GB consisting of (002)/(111) ATGBs and several one–atomic layer  $(\overline{111})/(002)$  steps. Shear stress was then applied to the bottom grain, as indicated by the white arrow. (**B**) The (002)/(111) ATGB facets migrated via the lateral motion of ( $\overline{111}$ )/(002) steps until a  $\Sigma$ 11 (113) STGB facet was formed at the right side of GB. Yellow arrows indicate GB migration directions. (**C**) The (002)/(111) ATGB and  $\Sigma$ 11 (113) STGB facets migrated jointly until another STGB facet was formed at the left side of GB. (**D** to **H**) Sequential snapshots showing the back-and-forth GB plane reorientation and the reversible facet transformation between STGB and ATGB facets at the left end (D to F) and the right end (F to H) of GB. The red dashed lines in (B) to (H) represent the initial GB position in (A). (**I** and **J**) Closer observation on the core structure of ( $\overline{111}$ )/(002) steps and the structure of  $\Sigma$ 11 (113) STGB. (**K**) Plots of the average GB inclination angle and the normalized facet ratio of (002)/(111) ATGB,  $\Sigma$ 11 (113) STGB, and ( $\Sigma$ 11 (113) STGB facet exists when the average inclination is larger than 15° (indicated by the black dashed line). Scale bars, (A to H) 2 nm and (I and J) 0.5 nm.

the motion of  $(\overline{11}1)_1/(002)_2$  step. As shown in the trichromatic pattern in fig. S7, from the topological perspective, the  $(111)_2$ -to- $(002)_1$  plane transformation involves the movement of atoms both in and out of the projective plane [i.e.,  $(1\overline{1}0)$  plane], while only in-plane adjustment of localized atoms is needed to accomplish the steps-to- $\Sigma 11(113)$  STGB transformation.

Considering that HRTEM images are essentially phase-contrast images, deducing the position of the atoms at GBs from HRTEM images might bring some uncertainty (section S1). Hence, MD simulations were carried out to reproduce the facet transformation process and to validate that the motion and coalescence of  $(\overline{111})_1/$ 

 $(002)_2$  steps led to the transformation. We constructed the zig-zag GB containing  $\{002\}/\{111\}$  facets and traced its structural evolution under the shear deformation (see Materials and Methods). Note that stacking faults (SFs) exist at the as-constructed GB as a consequence of structural relaxation (fig. S18C). The nucleation and subsequent motion of  $(\overline{11})_1/(002)_2$  steps and the formation of a  $\Sigma 11(113)$  STGB were captured at the zig-zag GB (Fig. 2, E to H, and fig. S18C), which agrees well with our experimental results and shows that the formation of the STGB could be the product of the coalescence of  $(\overline{11})/(002)$ -type steps. It should be mentioned that the intersection of SF with GB in the simulations serves the same

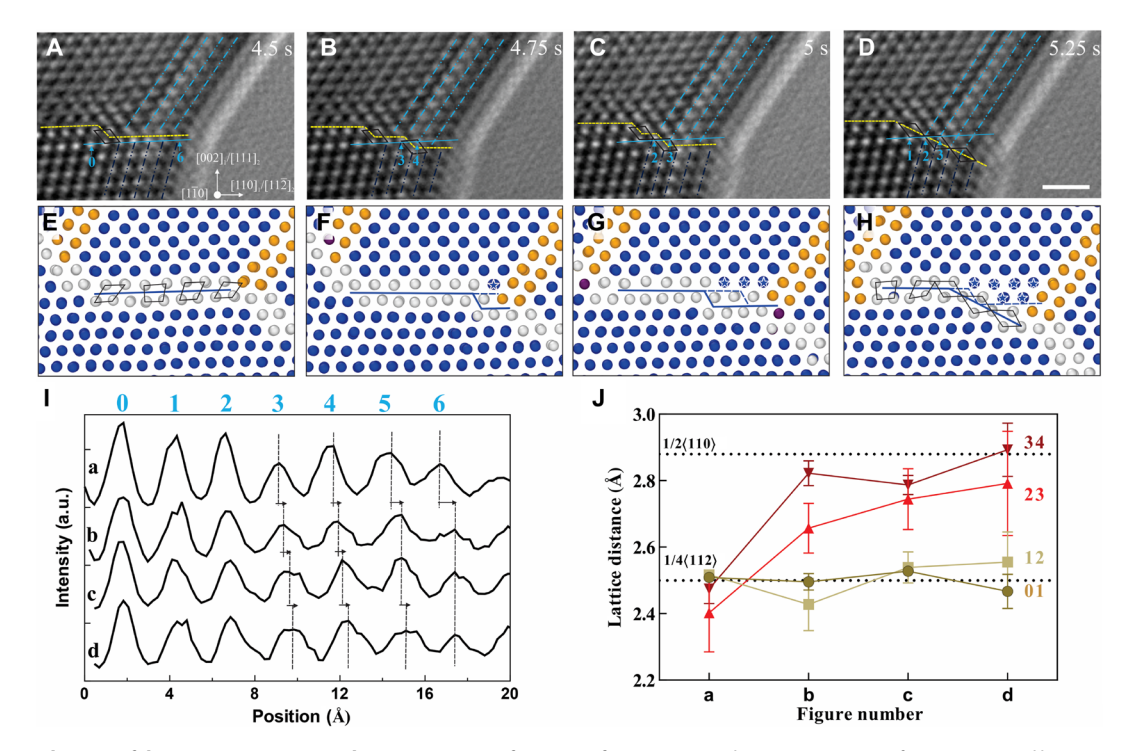


Fig. 2. Atomistic mechanism of the (002)/(111) ATGB to the  $\Sigma$ 11(113) STGB facet transformation. (A) The (002)/(111) ATGB facets connected by a preexisting ( $\overline{111}$ )/(002) step. (B to D) Sequential snapshots showing the nucleation and lateral motion of another ( $\overline{111}$ )/(002) step on the (002)/(111) ATGB and the formation of a  $\Sigma$ 11(113) STGB facet at the right corner of GB. (E to H) MD simulation showing the same (002)/(111) ATGB-to- $\Sigma$ 11(113) STGB facet transformation process as the experimental observation. In all MD simulation results, the blue, orange, and gray atoms indicate the FCC structure, hexagonal close-packed structure, and other coordination structure (i.e., GB structure), respectively. The blue dashed lines in (F) to (H) represent the positions of GB in the previous snapshot. The polygons in (E) and (F) indicate that (002)/(111) ATGB consists of face-sharing distorted C-type structure units, whereas  $\Sigma$ 11(113) STGB consists of corner-sharing C-type structure units (13). (I) The contrast intensity line profiles extracted from (A) to (D) at the same area as indicated by the blue solid line in (A). Atom columns are numbered from 0 to 6. a.u., arbitrary units. (J) Plot of the lattice spacing between atom columns 0, 1, 2, 3, and 4 in (A) to (D). Two dotted lines indicate the ideal length of  $\frac{1}{2}\langle 110 \rangle$  (2.88 Å for Au) and  $\frac{1}{4}\langle 112 \rangle$  (2.5 Å for Au), respectively. Scale bar, 1 nm.

role as the intersection of free surface with the GB in the experiments since they both act as the nucleation sites of  $(\overline{11}1)_1/(002)_2$  steps. A similar ATGB-to-STGB transformation was observed at the left side of the GB during the subsequent deformation in the experiment (fig. S8, A to D).

The as-formed  $\Sigma 11(113)$  STGB did not always migrate jointly with the (002)<sub>1</sub>/(111)<sub>2</sub> ATGB. It transformed back into the ATGB in some cases (Fig. 3). Figure 3A shows a flat  $\Sigma$ 11(113) STGB that was formed during the GB migration process. Under further shear loading, part of this STGB transformed into the serrated GB consisting of  $(002)_1/(111)_2$  ATGB facets and  $(\overline{11}1)_1/(002)_2$  steps (Fig. 3B). These steps moved on the ATGB along the  $[11\overline{2}]$  direction of the bottom grain G2, causing the backward migration of ATGB toward the upper grain G1 and triggering the transformation of the rest of the STGB into the ATGB (Fig. 3C). Moreover, as shown in the intensity profiles in Fig. 3G, a new intensity peak was found to emerge between peaks 4 and 5 during the STGB-to-ATGB transformation. This change is believed to be the direct result of (002)<sub>1</sub>-to-(111)<sub>2</sub> plane transformation after the GB migration since the structural repeat distance of (002)/(111) ATGB is ~1.88 nm for Au, which means that ~7 atomic columns in the (002)<sub>1</sub> plane match ~8 atomic columns in the  $(111)_2$  plane as shown in Fig. 3D. The  $(002)_1$ -to- $(111)_2$  plane transformation involves complex atom rearrangement, i.e., shuffling (fig. S9). The change in alignment between the two grains is a direct

consequence of the slight misorientation angle change during the transformation from 50.48° in the STGB to 54.74° in the ATGB, which is highlighted by the red horizontal dashed lines in Fig. 3D. Additional analysis on the change of lattice spacing from columns 2 to 6 (Fig. 3H) further supports the  $(002)_1$ -to- $(111)_2$  plane transformation mediated by the motion of step: The lattice spacings of 23 and 34 in Fig. 3 (A to C) remain in the value of ~2.5 Å, while the lattice spacing of 45 increases to a value far larger than 2.88 Å, and that of 56 fluctuates around 2.88 Å in Fig. 3B (i.e., the formation of a step between atom columns 4 and 5). Then, both of the lattice spacings of 45 and 56 dropped to ~2.5 Å in Fig. 3C [i.e., the completion of the  $(002)_1$ -to- $(111)_2$  plane transformation].

This reversed facet transformation process was also observed in our MD simulations. As shown in Fig. 3D, a disconnection was found on the STGB before the start of the transformation. Afterward, several step-connected  $(002)_1/(111)_2$  ATGBs were formed and extended via the lateral motion of the steps (Fig. 3, E and F), which is consistent with our experimental results. It is worth mentioning that there is no appearance of new atom columns in the simulations because the movement of  $(\overline{11}1)_1/(002)_2$  step in the simulations did not reach the structural repeat distance of  $(002)_1/(111)_2$  ATGB (39). Topological analysis on the atomic motion during this process shows that the different movement behaviors of the neighboring atoms near the  $\Sigma 11(113)$  STGB led to the facet transformation of the  $\Sigma 11(113)$ 

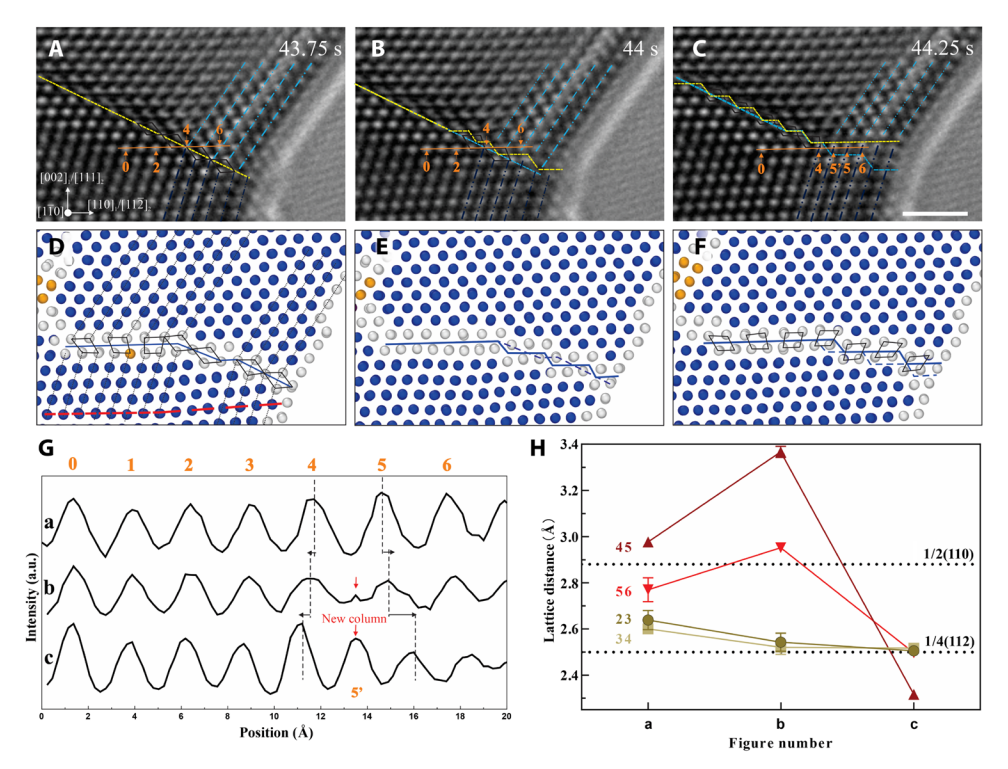


Fig. 3. Atomistic mechanism of the backward facet transformation from the Σ11(113) STGB to the (002)/(111) ATGB. (A) A long and flat Σ11(113) STGB facet, where the structure units are indicated by the rhombuses in dark. (B) Part of the Σ11(113) STGB transformed into several (TT1)/(002) steps connecting the (002)/(111) ATGBs. (C) More (TT1)/(002) steps were formed, and GB migrated backward via the lateral motion of (TT1)/(002) steps toward the free surface on the right. The identification of these steps is based on the translational displacements between (111)₁ planes (blue dashed-dotted lines) and (11T)₂ planes (purple dashed-dotted lines) at the GB. (D to F) MD simulation showing a similar backward facet transformation process as the experimental observation. The polygons in (D) and (F) indicate that (002)/(111) ATGB consists of face-sharing distorted C-type structure units, whereas Σ11(113) STGB consists of corner-sharing C-type structure units (13). (G) The contrast intensity line profiles extracted from (A) to (C) at the same area as indicated by the orange solid line in (A). Atom columns are numbered from 0 to 6. (H) Plot of lattice spacing between atom columns 2, 3, 4, 5, and 6 in (A) to (D). Some error bars are too short to show in the plot. The lattice spacing of 45 and 56 in (C) means the average lattice spacing of 45' and 5'5, respectively. Scale bar, 2 nm.

STGB into the stepped  $(002)_1/(111)_2$  ATGB (fig. S7C). A similar STGB-to-ATGB facet transformation was also observed at the other side of this bicrystal (fig. S8, E to G), which is believed to follow the same manner as described above. The reversed facet transformation and corresponding migration process should be a metastable state during the GB migration process under this specific shear loading condition, as the GB migration direction is opposite to the overall migration direction among the entire process. Thereby, this reversed migration of  $(002)_1/(111)_2$  ATGBs toward the upper grain G1 ceased soon, and the GB migration returned via the lateral motion of  $(\overline{111})_1/(002)_2$  steps along the  $[\overline{112}]$  direction of the bottom grain G2 or even transforming into the  $\Sigma 11(113)$  STGB again (fig. S10).

#### **GB** dissociation during migration

In addition to the faceted GB consisting of  $(002)_1/(111)_2$  ATGB and  $(\overline{11})_1/(002)_2$  steps as shown in Fig. 1A, a  $[\overline{110}]$  tilt bicrystal containing a faceted GB consisting of  $(002)_1/(111)_2$  ATGB (also confirmed by the structure unit analysis in fig. S1D) and  $(111)_1/(11\overline{1})_2$  facets was fabricated and tested (Fig. 4A and movie S2). Note that there were several SFs that dissociated from the GB into grain 1 at the areas near the facet junctions, which might serve to accommodate the misorientation deviation of this bicrystal from that of the ideal (002)/(111) ATGB (i.e., 56° versus 54.74°) (13, 40). Upon shearing,

the  $(111)_1/(11\overline{1})_2$  facets either decomposed into several  $(111)_1/(11\overline{1})_2$  $(11\overline{1})_2$  steps/nanofacets connecting the  $(002)_1/(111)_2$  ATGBs [see section S1 for the identification of these steps and fig. S11 for comparison with those  $(\overline{111})_1/(002)_2$  steps in Figs. 1 to 3] or moved as a whole (Fig. 4, B and C), causing the migration of some ATGB facets. The preexisting SFs seem to have little impact on the GB migration (Fig. 4, A and B) and even disappeared in the subsequent deformation (Fig. 4, C to F). One possible reason is that these SFs would contract into the GB before the movement of the  $(111)_1/(11\overline{1})_2$  steps and even maintain the high-energy contracted state during the following migration (40). Moreover, new  $(111)_1/(11\overline{1})_2$  steps were nucleated at the free surface to facilitate the GB migration (Fig. 4D). A subgrain (denoted as grain 3) was then formed and bounded by a (002)<sub>1</sub>/(111)<sub>3</sub> ATGB, the left-side free surface, and two newly formed GBs (Fig. 4E). These two GBs are identified as  $\Sigma 11(113)$  STGB (between grains 1 and 3) and  $\Sigma 3(111)$  STGB (between grains 2 and 3), which are both dissociated from the original faceted GB. The following growth of the subgrain was via the extension of the  $(002)_1$ /  $(111)_3$  ATGB and the migration of the  $\Sigma 11(113)$  STGB (Fig. 4F). A slight grain rotation occurred during this shear deformation, causing the misorientation angle to gradually increase to ~58° (fig. S6, E to G). In addition, the misorientation angle between grains 1 and 3 is ~51.5°, close to that in Fig. 1G and within the range of 50.48° to 54.74°

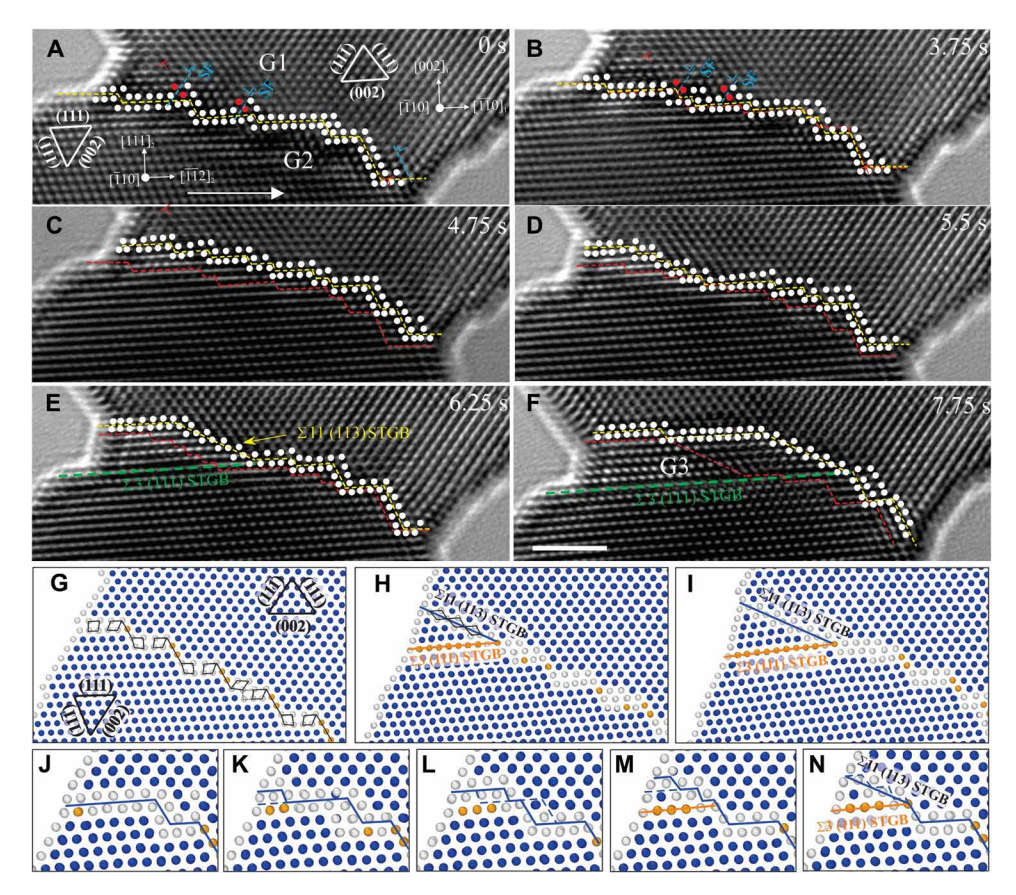


**Fig. 4. Shear-driven migration of another faceted GB coupled with GB dissociation.** (**A**) The structure of an as-fabricated Au bicrystal with a faceted GB composed of (002)/(111) ATGB and near (111)/(111) GB facets. Shear stress was then applied to the bottom grain, as indicated with the white arrow. (**B**) The (111)/(111) GB facets either decomposed into several one–atomic layer (111)/(111) steps or migrated via collective motion. (**C**) Further GB migration via lateral motion of (111)/(111) steps and collective motion of (111)/(111) GB facets. (**D**) (111)/(111) steps nucleated at the free surface and moved into the bicrystal. (**E**) The faceted GB dissociated into a Σ11 (113) STGB and a Σ3 (111) STGB. A subgrain region (grain 3) was formed. (**F**) The subgrain grew via the extension of (002)/(111) ATGB facets and migration of Σ11 (113) STGB. In (A) to (F), the yellow and the red dashed lines represent the current and the previous positions of the faceted GB, separately. Green dashed lines represent the newly formed Σ3 (111) STGB. (**G** to **I**) Sequential snapshots of MD simulations showing the same process as experimental observation of the formation and growth of a subgrain during the migration of a faceted GB consisting of (002)/(111) ATGB and (111)/(111) GB facets. The polygons in (G) and (H) indicate that (002)/(111) ATGB consists of face-sharing distorted C-type structure units, whereas Σ11(113) STGB consists of corner-sharing C-type structure units. (**J** to **N**) Detailed MD simulation results showing the dynamic GB dissociation process. Scale bar, 2 nm

[i.e., the misorientation angles for ideal  $\Sigma 11(113)$  STGB and (002)/ (111) ATGB]. Therefore, it is not unexpected to observe a serrated GB consisting of  $(002)_1/(111)_3$  ATGB and  $\Sigma 11(113)$  STGB facets between grains 1 and 3.

Similar to the  $(002)_1/(111)_2$  ATGB–to– $\Sigma 11(113)$  STGB facet transformation in Fig. 2, the GB dissociation, in this case, is highly related to the coalescence of steps connecting the  $(002)_1/(111)_2$  ATGB facets (Fig. 4, D and E), except that these steps are of  $(111)_1/(111)_2$  type. Although the  $\Sigma 11(113)$  STGB was formed in both cases, the underlying mechanisms are believed to be different, and Shockley partial dislocations are expected to be involved in the formation of  $\Sigma 3(111)$  STGB during the GB dissociation process. To explore the atomistic mechanism, MD simulations were carried out to reproduce this GB migration and dissociation process. The nucleation and growth of a subgrain, which is enclosed by a  $\Sigma 11(113)$  STGB and a  $\Sigma 3(111)$  STGB that were dissociated from the original GB structure during the migration process, were captured (Fig. 4, G to I). Specifically, the GB dissociation process is not a one-step event. The formation of  $\Sigma 3(111)$  STGB was found to be accompanied by the nucleation

and motion of  $(111)_1/(002)_3$  steps on the  $(002)_1/(111)_3$  ATGB facet. Afterward, those  $(111)_1/(002)_3$  steps coalesced and transformed into a  $\Sigma 11(113)$  STGB (Fig. 4, J to N), the same as that in Fig. 2. In addition, the subgrain growth is assisted by the motion of a triple junction, where the  $\Sigma 3(111)$  STGB keeps stationary, but the  $\Sigma 11(113)$  STGB and the rest of the original serrated GB moved roughly rightward (fig. S12).

#### **DISCUSSION**

GB faceting is believed to be a process to minimize the total GB free energy (41). As a prevalent type of GB in polycrystalline materials, ATGBs are normally found to facet into low-energy STGBs or facets with at least one {111} low-index plane on two sides of the GB in FCC metals (31, 41). In our results, (002)/(111) ATGB is found to mainly combine with ( $\overline{111}$ )/(002) ATGB, (111)/(11 $\overline{1}$ ) GB, or  $\Sigma$ 11(113) STGB to form a faceted GB structure. Note that (111)/(11 $\overline{1}$ ) GB (i.e., coherent twin boundary) and  $\Sigma$ 11(113) STGB are the two lowest-energy GBs among [110] tilt GBs, while (002)/(111) ATGB has a

slightly higher energy than the  $\Sigma 11(113)$  STGB (33). During the shear loading, the two different types of faceted GB structure would undergo dynamic GB structural transformation, and both transform into the faceted GB consisting of (002)/(111) ATGB and  $\Sigma 11(113)$  STGB, either via the direct facet transformation (Fig. 1) or GB dissociation (Fig. 4).

Regarding the reversible facet transformation that occurred between (002)/(111) ATGB and  $\Sigma$ 11(113) STGB during the migration of faceted GB containing (002)/(111) and  $(\overline{11}1)/(002)$  facets (Fig. 1), it is now clear that the ATGB-to-STGB facet transformation can be accomplished through the coalescence of  $(\overline{111})/(002)$  steps (Fig. 2), while the backward STGB-to-ATGB transformation happens via the detachment of  $(\overline{111})/(002)$  steps from the STGB and the subsequent motion of these steps (Fig. 3). The specific shear loading parallel to the (002)<sub>1</sub>/(111)<sub>2</sub> ATGB in our experiment (Fig. 1) seems to activate the transformation: On the one hand, it promotes the nucleation and motion of  $(\overline{111})/(002)$  steps. Those steps are necessary for the ATGB-to-STGB transformation; on the other hand, it has a large inclination angle (~25°) with the as-formed STGB facets, making those STGB facets easy to decompose back into steps during subsequent migration. To better understand the influence of loading conditions on the facet transformation, we examined the mechanical responses of (002)/(111) ATGB and  $\Sigma$ 11(113) STGB under different loading conditions. The ATGB is found to easily transform to STGB under all tested loading conditions, including compressive loading perpendicular to the ATGB (Fig. 5, A to D, and movie S3), shear loading with an inclination angle of ~30° from the ATGB (Fig. 5, E to H, and movie S4), and shear loading nearly parallel to the ATGB as shown in Fig. 1. The strong tendency of the ATGB-to-STGB transformation is possibly because it is a thermodynamically favorable process (fig. S4). In comparison, whether the STGB-to-ATGB transformation happens depends on the angles between the shear loading and the STGB. Only when the angle is larger than ~14° (Fig. 6I), obvious STGB-to-ATGB transformation was observed during the migration (Fig. 6, E to H, and movie S5). Otherwise, the mechanical response of STGB would be simply disconnection-mediated migration (Fig. 6, A to D, and movie S6) (30).

To further elucidate the loading dependence of the STGB-to-ATGB transformation, we apply Pond's topological theory of bicrystal crystallography (42, 43) to analyze the Burgers vector for an ideal oneatomic layer( $\overline{11}1$ )/(002) step on the (002)/(111) ATGB (section S4, fig. S14, and table S2). Our analysis shows that the  $(\overline{11}1)/(002)$  step contains the edge component  $\mathbf{b}_{\rm e}$  [|  $\mathbf{b}_{\rm e}$ | =  $(2\sqrt{6} - 3\sqrt{2}) a/12$ , a is the lattice parameter of Au and the screw component  $\mathbf{b}_{s}$  ( $|\mathbf{b}_{s}| = \sqrt{2} a/4$ ) that are parallel to the ATGB plane and accommodate the GB migration as the step moves on the ATGB and the normal component  $\mathbf{b}_{\rm n}$  [ $|\mathbf{b}_{\rm n}| = (2\sqrt{3} - 3)a/6$ ] that is perpendicular to the ATGB plane but can move conservatively along the step to complete the GB migration (43). In comparison, the Burgers vectors of the disconnections of  $\Sigma 11(113)$  STGB are known to be all parallel to the STGB plane (30, 43). Therefore, it is likely that the relative magnitude of resolved shear stress on the STGB plane and the ATGB plane determines whether the STGB-to-ATGB transformation would happen, as the critical angle of ~14° is close to the half of the angle between STGB and ATGB (i.e., 25.2°). It needs to mention that the critical angle of loading dependence was determined in bicrystals without the constraints from neighboring grains. In nanograined materials, the stress/strain state in local region could be different from the external loading; thus, the critical angle could be different.

We notice that the reversible facet transformation essentially starts from a faceting/defaceting process at atomic scale if we treat those steps as  $(\overline{11}1)/(002)$  nanofacets (Fig. 11). Specifically, the ATGB-to-STGB facet transformation corresponds to a defaceting process of a faceted GB consisting of equal-length (002)/(111) and  $(\overline{11}1)/(002)$ nanofacets into a complete  $\Sigma 11(113)$  STGB, and the backward facet transformation is a faceting process starting from the STGB into the same faceted GB (Fig. 7I). Revisiting the simulation results, we found that these faceting/defaceting transformations took place frequently (Fig. 7, A to H) and should be a general phenomenon between  $\Sigma$ 11(113) STGB and (002)/(111)-type nanofacets. This faceting/ defaceting process is analogous to the nucleation and annihilation of disconnection dipoles on  $\Sigma 11(113)$  STGB (Fig. 7J), as all the singlelayer, double-layer, or four-layer disconnections reported in literature contain the  $(\overline{11}1)/(002)$ -type nanofacets (30). Hence, the loading condition dependence of the STGB-to-ATGB transformation can be well explained: The external loading influences whether the  $(\overline{1}\overline{1}1)/(002)$  nanofacets form after initial faceting moves on the  $\Sigma$ 11(113) STGB or on the (002)/(111) ATGB, i.e., different Burgers vectors, which consequently determines whether the  $\Sigma 11(113)$  STGB undergoes the conservative migration (Figs. 6, A to D, and 7J) or the STGB-to-ATGB facet transformation (Fig. 6, E to H, and 7K).

It is also noticed that the reversible facet transformation predominately occurred at the region near the edge free surface in our nano-bicrystals due to the lack of constrains (Fig. 1). The edge free surface acts as the nucleation source of steps (Fig. 2B) and accommodates the mutual transition between  $\Sigma 11(113)$  STGB and (002)/ (111) ATGB (Figs. 2, A to D, and 3, A to C). In polycrystalline materials, other nucleation sources and strain accommodation mechanisms are needed. As shown in Figs. 5 and 6 (F to H), GB junctions (30, 44) that commonly exist in polycrystalline materials can be effective sites that promote the nucleation of  $(\overline{111})/(002)$  steps and coordinate the ATGB-to-STGB (Fig. 5) and the STGB-to-ATGB transformations (Fig. 6, F to H). The GB facet junction (45) and the intersection of SF with GB (as evidenced by the simulation results in Fig. 2, E to H) can also play a similar role as GB junctions in polycrystalline materials. Moreover, only a very localized atom adjustment is needed to accommodate the facet transformation (Figs. 2 and 3 and fig. S7), which could be sufficiently accommodated by the lattice distortion of grains in polycrystalline materials. One example is that the STGB-to-ATGB transformation is also found in regions far from the side free surface (fig. S13, C and D). Given that  $\Sigma 11(113)$  STGB and (002)/(111)ATGB are found to be preserved as much as possible in the GBs vicinal to these special geometrics, such as 52.9° [110] tilt GB (31), and GB faceting is also prevalent in various types of GBs (table S3) (24, 31, 32, 40, 45-55), it is thus reasonable to believe that the faceting/ defaceting process and resultant facet transformation mechanisms discussed here could have a general implication to the understanding of the structural evolution of faceted GBs during stress-driven migration in nanocrystalline or polycrystalline materials (additional examples of stress-driven facet transformation can be found in figs. S15 and S16).

For the faceted GB constructed by (002)/(111) ATGB and near  $(111)/(11\overline{1})$  GB facets, GB dissociation, instead of direct facet transformation, was found during the migration process (Fig. 4). This distinction is originated from the different structure features of the steps mediating the migration of (002)/(111) ATGB facets (fig. S11). On the one hand, there is no low-energy interface comparable to the  $\Sigma 11(113)$  STGB that can be formed via the direct coalescence of  $(111)/(11\overline{1})$  steps or defaceting process in this case. Consequently,

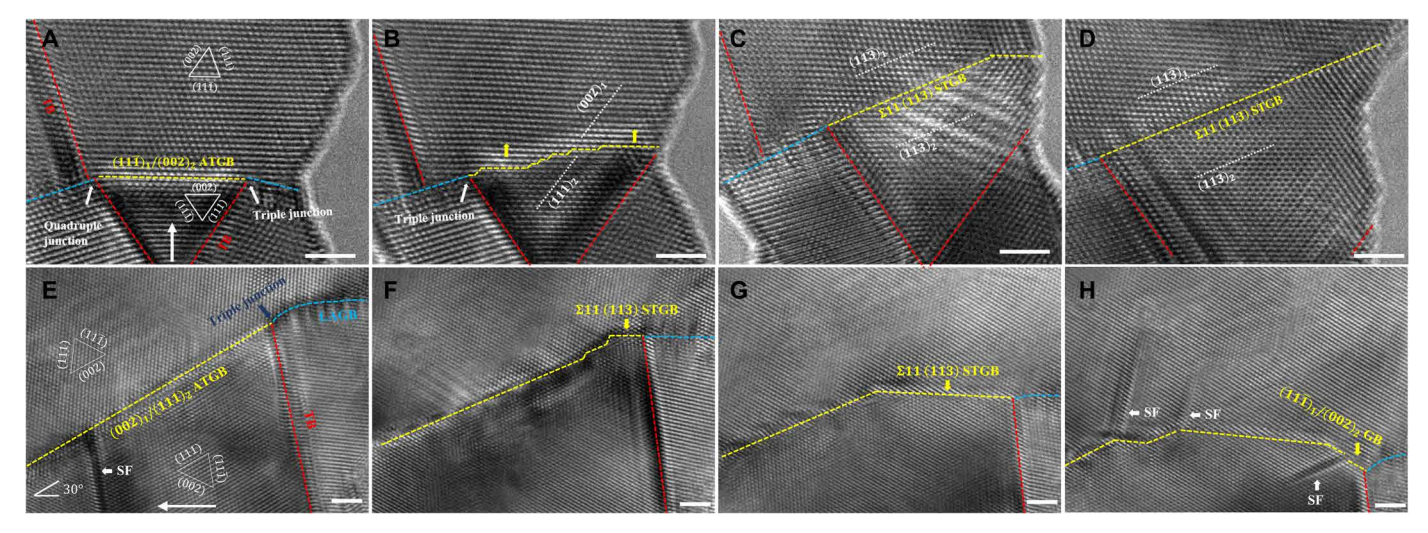


Fig. 5. Transformations of {002}/{111}-type ATGB into Σ11 (113) STGB under different loading conditions. (A to D) A flat (11 $\overline{1}$ )/(002) ATGB bounded by two GB junctions transformed into the Σ11 (113) STGB under the compressive loading perpendicular to the ATGB. Similarly, the ATGB-to-STGB transformation is via the nucleation and coalescence of (002)/(111) steps. (**E** to **H**) (002)/(111) ATGB-to-Σ11 (113) STGB transformation started from a GB triple junction. Shear loading with an inclination angle of ~30° was applied as indicated by the white arrow. Note that all the grains rotated clockwise due to the rigid body rotation of the whole system, but the average misorientations for the (002)/(111) ATGB do not change substantially, i.e., 52.67°, 53°, and 54° in (E) to (H). Scale bars, 2 nm.

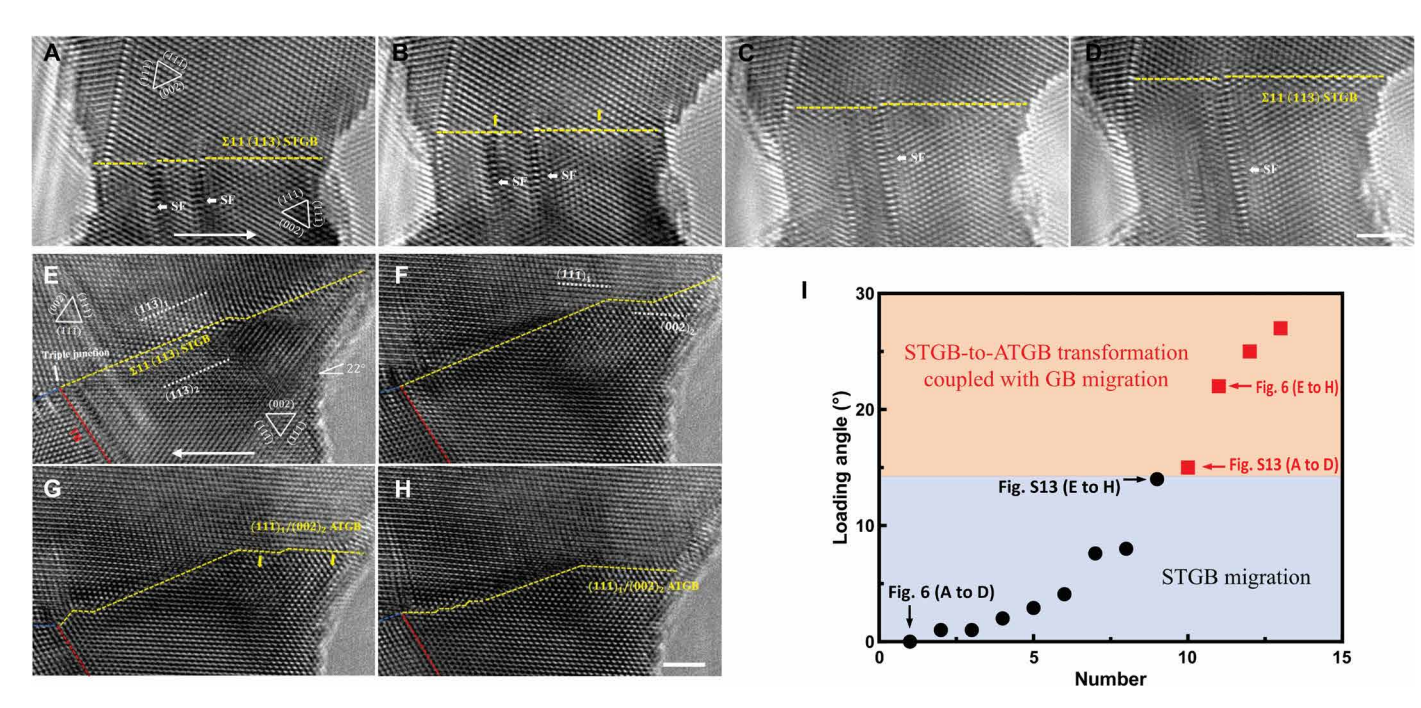


Fig. 6. The loading direction dependence of Σ11 (113) STGB-to-{002}/{111} ATGB transformation. (A to D) Conservative migration of Σ11 (113) STGB mediated by disconnections. Shear loading was near parallel to the STGB as indicated by the white arrow in (A). (E to H) STGB-to-ATGB transformation occurred when the STGB had an inclination angle of ~22° with the shear loading direction. The STGB-to-ATGB transformation is coupled with the migration of both the ATGB and the STGB. (I) Plot of loading angle between STGB and applied shearing versus the experimental number. Black balls indicate the disconnection-mediated migration of STGB, while red cubes mean that the STGB-to-ATGB transformation happened during the migration process. An additional example can be found in fig. S13. Scale bars, 2 nm.

this kind of faceted GB tends to dissociate into the two lower-energy interfaces, i.e.,  $\Sigma 11(113)$  STGB and  $\Sigma 3(111)$  STGB, during the migration process. On the other hand, the Burgers vector for the  $(111)/(11\overline{1})$  step is different from that for the  $(\overline{11}1)/(002)$  step. It has only the edge component  $\mathbf{b}_e$  [ $|\mathbf{b}_e| = (3\sqrt{2} - \sqrt{6})a/12$ ] and the normal component  $\mathbf{b}_n$  [ $|\mathbf{b}_n| = (2\sqrt{3} - 3)a/6$ ]. The emission of a

mixed-type partial dislocation can compensate the difference between the Burgers vectors of the (111)/(11 $\overline{1}$ ) step and the ( $\overline{11}$ 1)/(002) step (section S4). In addition, this GB dissociation behavior can be interpreted on the basis of the coincidence site lattice (CSL) GB model. In cubic polycrystals, CSL GBs are classified by a  $\Sigma$  value, which means the reciprocal coincidence site density, and the

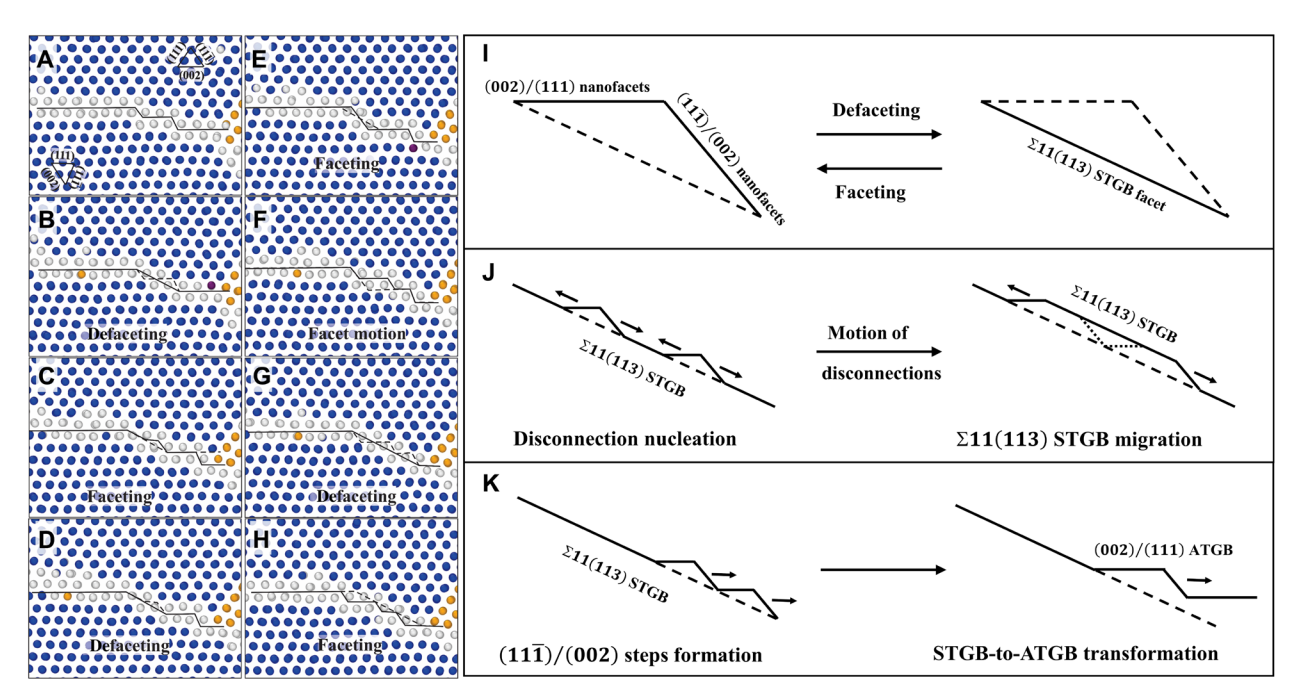


Fig. 7. Atomistic mechanisms of the loading direction dependence of STGB-to-ATGB transformation. (A to H) MD simulation snapshots showing the frequent faceting/defaceting transformation between the  $\{002\}/\{111\}$ -type nanofacets and the  $\Sigma$ 11 (113) STGB. (I) Schematic illustration showing the faceting/defaceting transformation. (J) Disconnection-mediated migration of  $\Sigma$ 11 (113) STGB after initial faceting (i.e., nucleation and motion of disconnection dipoles). (K) STGB-to-ATGB transformation via the motion of  $(11\overline{1})/(002)$  steps formed after initial faceting.

dissociation of CSL GBs is believed to follow the so-called "\$\Sigma\$ combination rule" (56). For instance, \$\Sigma 27 \rightarrow \Sigma 3 + \Sigma 9\$ and \$\Sigma 9 \rightarrow \Sigma 3 + \Sigma 3\$ (57). In our case, the faceted GB has a misorientation angle of ~58° (fig. S6G), very close to the ideal value of \$\Sigma 33\$ GB (i.e., 59°) (31). Therefore, the GB dissociation reaction here is essentially: \$\Sigma 33\$ faceted GB \rightarrow \Sigma 3(111)\$ STGB + \$\Sigma 11(113)\$ STGB. It should be mentioned that the existence of the free surface might promote the GB dissociation (58), but it is not an indispensable condition because the GB dissociation behavior also happens in a restricted environment (i.e., region away from the free surface; see fig. \$17), and shear-coupled GB migration accompanied by the formation of twins is also common during the deformation of FCC polycrystals (59).

Moreover, our findings may provide a plausible atomistic understanding of the coincreased proportion of  $\Sigma 11$  and  $\Sigma 3$  GB after the cyclic deformation of nanocrystalline FCC metals (4), as any ATGBs with a misorientation angle vicinal to 54.74° could contain the (002)/ (111) facets in their GB structure, which would directly transform into the  $\Sigma 11(113)$  STGB (Fig. 2) or dissociate into a  $\Sigma 11(113)$  STGB and a  $\Sigma 3(111)$  STGB (Fig. 4) during the stress-driven GB migration process. Furthermore, our work enriches the understanding of the complexity of GB migration, as it clearly shows that GB structure is in a metastable state during the migration, where mutual transformations occur between the stable GB facets such as (002)/(111)-type ATGBs, Σ11(113) STGB, and Σ3(111) STGB. These transformations would cause the change of GB crystallography (i.e., misorientation and inclination) and affect the direction and speed of GB migration. In our case, the  $\Sigma$ 11 (113) STGB migrates faster than the (002)/(111) ATGB, which is supported by our observations that the right part of the GB moved more atomic layers than its left part in Fig. 1 (A to H), and the width of the subgrain grows much faster than its height in Fig. 4 (E and F). The dynamic GB structural transformation during the migration process and the resulted migration speed discrepancies between different GB facets may be the reason for stress-driven directional fast grain growth in nanocrystalline metals (2, 3, 60). In addition, our work emphasizes the importance of faceting/defaceting mechanism on GB migration and facet transformations and thus could serve a role to bridge the disconnection-mediated GB migration and the GB structural transformation resulted from GB complexion transition.

In conclusion, the dynamic GB structural transformations during the stress-driven migration of two different faceted ATGBs both containing (002)/(111) facets have been revealed using the in situ HRTEM technique combined with MD simulations. A low-energy  $\Sigma$ 11(113) STGB was found to form in both cases, via either facet transformation or GB dissociation. The core structure of steps,  $(\overline{111})/(002)$  type or  $(111)_1/(11\overline{1})_2$  type, connecting the (002)/(111)facets determine which pathway it tends to follow. In addition, the facet/defaceting transformation between Σ11(113) STGB and (002)/ (111)-type nanofacets appears to be the origin of the reversible facet transformation. Whether the  $\Sigma 11(113)$  STGB after initial faceting would migrate conservatively or transform into the (002)/(111) ATGB depends on the loading condition. Given that any GBs vicinal to these two special geometrics potentially have a GB structure similar to what we have observed and GB faceting is commonly observed in various types of GBs, the GB structural transformation mechanisms proposed here should have a general implication to the deformation-induced GB structural evolution of faceted GBs. The discovery of dynamic GB structural transformation during the shear-mediated migration will enrich our understanding of the complexity of GB migration and have an impact on the development of nanocrystalline materials with microstructure control through thermal-mechanical processing.

#### **MATERIALS AND METHODS**

#### In situ nanowelding and shear testing

In situ nanowelding and shear testing of Au bicrystals were performed inside an FEI Titan Themis G2 200 probe Cs-corrected STEM using a Nanofactory scanning tunneling microscope (STM) holder. The metals used in this work are high-purity (99.999%) Au wires ordered from ESPI Metals. Before the in situ experiments, bulk Au wires were cut by a wire cutter to obtain the clean fracture surface with plenty of nanotips, which were then loaded onto the static side and the probe side of the STM holder. The sharp nanotips of Au with a certain misorientation angle in the (110) zone axis were selected to be welded together to fabricate bicrystals with different GBs. Before welding, a constant voltage of ~2 V was applied on the probe side. Subsequently, two selected nanotips melted and formed a bicrystal at the moment of contact. The in situ shear testing was controlled by moving the probe side with the piezo-manipulator of the STM holder at a constant rate between 0.001 and 0.01 nm s<sup>-1</sup>. All the in situ experiments were operated at 200 kV, and low-dose beam conditions (the electron density < 10<sup>5</sup> A m<sup>-2</sup>) were used to minimize the potential beam effects on GB migration behaviors. In addition, all the in situ experiments were recorded in real time by a charge-coupled device camera at a frame rate of 0.25 s per frame.

#### **MD** simulations

MD simulations were performed on a Au bicrystal structure using the Large-scale Atomic/Molecular Massively Parallel simulation (61) and embedded atom method potential (62) for Au. For constructing zig-zag (002)/(111) ATGB, we first constructed a (10 10 7)/(10 10  $\overline{7}$ ) STGB by joining two separate orthogonal crystal lattices along the  $\langle 10\ 10\ 7 \rangle$  direction as shown in (fig. S18A). Then, the  $(10\ 10\ 7)/(10\ 10\ \overline{7})$ STGB was optimized at 300 K under zero pressure with an isothermalisobaric (constant number of particles, pressure, and temperature, or NPT) ensemble to obtain the equilibrium zig-zag (002)/(111) ATGB (fig. S18C). For faceted GB consisting of  $(111)/(11\overline{1})$  STGB and (002)/(111)(111) ATGB, we first constructed a (113)/(771) ATGB by joining two separate orthogonal crystal lattices along the (113) and (771) direction (fig. S18B). Then, the (113)/(771) ATGB were optimized at 300 K using NPT ensemble (fig. S18D). Periodic boundary conditions were applied along all the directions under structural optimization. In the shear deformation, a constant shear velocity of 1 m s<sup>-1</sup> parallel to the GB plane at the temperature of 300 K was applied on a fixed area of the top grain along the  $\langle 7 7 20 \rangle$  direction for  $(10\ 10\ 7)/(10\ 10\ \overline{7})$ STGB or along the (332) direction for (113)/(771) ATGB (fig. S18). Periodic boundary conditions were applied along the (110) tilt direction, and the canonical (constant number of particles, volume, and temperature, or NVT) ensemble was used in this case. The obtained atomic structures were analyzed using OVITO (63). Models with free boundary conditions along the (110) tilt direction and different thicknesses (e.g., up to 5.7 nm) were also tested, and we observed no influence from the boundary condition or GB thickness on the simulation results.

#### **SUPPLEMENTARY MATERIALS**

Supplementary material for this article is available at https://science.org/doi/10.1126/sciadv.abn3785

#### **REFERENCES AND NOTES**

- L. Priester, Grain Boundaries: From Theory to Engineering (Springer Science & Business Media, 2012), vol. 172.
- M. Legros, D. S. Gianola, K. J. Hemker, In situ TEM observations of fast grain-boundary motion in stressed nanocrystalline aluminum films. Acta Mater. 56, 3380–3393 (2008).

- F. Mompiou, D. Caillard, M. Legros, Grain boundary shear–migration coupling—I. In situ TEM straining experiments in Al polycrystals. Acta Materialia 57, 2198–2209 (2009).
- J. F. Panzarino, Z. Pan, T. J. Rupert, Plasticity-induced restructuring of a nanocrystalline grain boundary network. Acta Mater. 120, 1–13 (2016).
- C. A. Schuh, M. Kumar, W. E. King, Analysis of grain boundary networks and their evolution during grain boundary engineering. Acta Mater. 51, 687–700 (2003).
- T. J. Rupert, D. S. Gianola, Y. Gan, K. J. Hemker, Experimental observations of stress-driven grain boundary migration. Science 326, 1686–1690 (2009).
- J. W. Cahn, J. E. Taylor, A unified approach to motion of grain boundaries, relative tangential translation along grain boundaries, and grain rotation. *Acta Mater.* 52, 4887–4898 (2004).
- J. W. Cahn, Y. Mishin, A. Suzuki, Coupling grain boundary motion to shear deformation. Acta Mater. 54, 4953–4975 (2006).
- S. E. Babcock, R. W. Balluffi, Grain boundary kinetics—II. In situ observations of the role
  of grain boundary dislocations in high-angle boundary migration. Acta Metall. 37,
  2367–2376 (1989).
- J. Han, S. L. Thomas, D. J. Srolovitz, Grain-boundary kinetics: A unified approach. Prog. Mater. Sci. 98, 386–476 (2018).
- C. M. F. Rae, D. A. Smith, On the mechanisms of grain boundary migration. *Philos. Mag. A.* 41, 477–492 (1980).
- V. Randle, Overview no. 127The role of the grain boundary plane in cubic polycrystals. Acta Mater. 46, 1459–1480 (1998).
- 13. M. J. McCarthy, T. J. Rupert, Emergence of directionally-anisotropic mobility in a faceted  $\Sigma 11 \langle 110 \rangle$  tilt grain boundary in Cu. *Model. Simul. Mater. Sci. Eng* **28**, 055008 (2020).
- M. J. McCarthy, T. J. Rupert, Shuffling mode competition leads to directionally anisotropic mobility of faceted Σ11 boundaries in fcc metals. *Phys. Rev. Mater.* 4, 113402 (2020)
- D. Caillard, F. Mompiou, M. Legros, Grain-boundary shear-migration coupling.
   II. Geometrical model for general boundaries. Acta Mater. 57, 2390–2402 (2009).
- F. Mompiou, M. Legros, D. Caillard, SMIG model: A new geometrical model to quantify grain boundary-based plasticity. Acta Mater. 58, 3676–3689 (2010).
- R. Hadian, B. Grabowski, C. P. Race, J. Neugebauer, Atomistic migration mechanisms of atomically flat, stepped, and kinked grain boundaries. *Phys. Rev. B* 94, 165413 (2016).
- Z. T. Trautt, A. Adland, A. Karma, Y. Mishin, Coupled motion of asymmetrical tilt grain boundaries: Molecular dynamics and phase field crystal simulations. Acta Mater. 60, 6528–6546 (2012).
- A. Rajabzadeh, M. Legros, N. Combe, F. Mompiou, D. A. Molodov, Evidence of grain boundary dislocation step motion associated to shear-coupled grain boundary migration. *Philos. Mag.* 93, 1299–1316 (2013).
- A. Rajabzadeh, F. Mompiou, S. Lartigue-Korinek, N. Combe, M. Legros, D. A. Molodov, The role of disconnections in deformation-coupled grain boundary migration. *Acta Mater.* 77, 223–235 (2014).
- V. Randle, Asymmetric tilt boundaries in polycrystalline nickel. Acta Crystallogr. A 50, 588–595 (1994).
- P. R. Cantwell, M. Tang, S. J. Dillon, J. Luo, G. S. Rohrer, M. P. Harmer, Grain boundary complexions. Acta Mater. 62, 1–48 (2014).
- M. S. Masteller, C. L. Bauer, Faceting of migrating (110) coincidence boundaries in aluminium bicrystals. *Philos. Mag. A* 38, 697–706 (1978).
- 24. K. L. Merkle, L. J. Thompson, F. Phillipp, In-situ HREM studies of grain boundary migration Interface Sci. 12, 277–292 (2004).
- J. Wei, B. Feng, R. Ishikawa, T. Yokoi, K. Matsunaga, N. Shibata, Y. Ikuhara, Direct imaging of atomistic grain boundary migration. *Nat. Mater.* 20, 951–955 (2021).
- T. Frolov, Effect of interfacial structural phase transitions on the coupled motion of grain boundaries: A molecular dynamics study. Appl. Phys. Lett. 104, 211905 (2014).
- L. Smith, D. Farkas, Non-planar grain boundary structures in fcc metals and their role in nano-scale deformation mechanisms. *Philos. Mag.* 94, 152–173 (2014).
- L. Zhang, C. Lu, K. Tieu, X. Zhao, L. Pei, The shear response of copper bicrystals with Σ11 symmetric and asymmetric tilt grain boundaries by molecular dynamics simulation. Nanoscale 7, 7224–7233 (2015).
- A. Bhattacharya, Y.-F. Shen, C. M. Hefferan, S. F. Li, J. Lind, R. M. Suter, C. E. Krill III, G. S. Rohrer, Grain boundary velocity and curvature are not correlated in Ni polycrystals. 374, 189–193 (2021).
- Q. Zhu, G. Cao, J. Wang, C. Deng, J. Li, Z. Zhang, S. X. Mao, In situ atomistic observation of disconnection-mediated grain boundary migration. *Nat. Commun.* 10, 156 (2019).
- K. L. Merkle, High-resolution electron microscopy of grain boundaries. *Interface Sci.* 2, 311–345 (1995).
- O. H. Duparc, S. Poulat, A. Larere, J. Thibault, L. Priester, High-resolution transmission electron microscopy observations and atomic simulations of the structures of exact and near Σ = 11, {332} tilt grain boundaries in nickel. *Philos. Mag. A* 80, 853–870 (2000).
- J. A. Brown, Y. Mishin, Dissociation and faceting of asymmetrical tilt grain boundaries: Molecular dynamics simulations of copper. *Phys. Rev. B* 76, 134118 (2007).

#### SCIENCE ADVANCES | RESEARCH ARTICLE

- D. L. Medlin, D. Cohen, R. C. Pond, Accommodation of coherency strain by interfacial disconnections at a 90° (110) grain boundary in gold. *Philos. Mag. Lett.* 83, 223–232 (2003).
- 35. O. Hardouinduparc, J.-P. Couzinié, J. Thibault-Pénisson, S. Lartigue-Korinek, B. Décamps, L. Priester, Atomic structures of symmetrical and asymmetrical facets in a near  $\Sigma = 9\{221\}$  tilt grain boundary in copper. *Acta Mater.* **55**, 1791–1800 (2007).
- J. D. Rittner, D. N. Seidman, (110) symmetric tilt grain-boundary structures in fcc metals with low stacking-fault energies. *Phys. Rev. B* 54, 6999–7015 (1996).
- K. L. Merkle, L. J. Thompson, F. Phillipp, High-resolution electron microscopy at a (113) symmetric thermally activated step motion observed by tilt grain-boundary in aluminium. *Philos. Mag. Lett.* 82, 589–597 (2002).
- K. L. Merkle, Atomic structure of grain boundaries. J. Phys. Chem. Solid 55, 991–1005 (1994).
- 39. K. L. Merkle, D. Wolf, Quasiperiodic features in the atomic structure of long-period grain boundaries. *Mater. Lett.* **17**. 217–222 (1993).
- M. L. Bowers, C. Ophus, A. Gautam, F. Lançon, U. Dahmen, Step coalescence by collective motion at an incommensurate grain boundary. *Phys. Rev. Lett.* 116, 106102 (2016)
- 41. H. U. Hong, H. W. Jeong, I. S. Kim, B. G. Choi, Y. S. Yoo, C. Y. Jo, Significant decrease in interfacial energy of grain boundary through serrated grain boundary transition.
- Philos. Mag. 92, 2809–2825 (2012).
  42. R. C. Pond, D. S. Vlachavas, Bicrystallography. Proc. R. Soc. Lond. A. 386, 95–143 (1983).
- J. P. Hirth, R. C. Pond, R. G. Hoagland, X. Y. Liu, J. Wang, Interface defects, reference spaces and the Frank–Bilby equation. *Prog. Mater. Sci* 58, 749–823 (2013).
- S. L. Thomas, C. Wei, J. Han, Y. Xiang, D. J. Srolovitz, Disconnection description of triple-junction motion. *Proc. Natl. Acad. Sci. U.S.A.* 116, 8756–8765 (2019).
- R. Hadian, B. Grabowski, M. W. Finnis, J. Neugebauer, Migration mechanisms of a faceted grain boundary. *Phys. Rev. Mat.* 2, 043601 (2018).
- S. B. Lee, W. Sigle, W. Kurtz, M. Rühle, Temperature dependence of faceting in Σ5(310) [001] grain boundary of SrTiO<sub>3</sub>. Acta Mater. 51, 975–981 (2003).
- T. E. Hsieh, R. W. Balluffi, Observations of roughening/de-faceting phase transitions in grain boundaries. *Acta Metall.* 37, 2133–2139 (1989).
- L. Wan, J. Li, Shear responses of -tilt {1 1 5}/{1 1 1} asymmetric tilt grain boundaries in fcc metals by atomistic simulations. Model. Simul. Mater. Sci. Eng. 21, 055013 (2013).
- Z. X. Wu, Y. W. Zhang, D. J. Srolovitz, Grain boundary finite length faceting. Acta Mater. 57, 4278–4287 (2009).
- F. Sansoz, J. F. Molinari, Mechanical behavior of Σ tilt grain boundaries in nanoscale Cu
- and Al: A quasicontinuum study. *Acta Mater.* 53, 1931–1944 (2005).
  51. S. B. Lee, H. N. Han, Faceting-roughening transition of a Cu grain boundary under electron-beam irradiation at 300 keV. *Sci. Rep.* 11, 15563 (2021).
- D. L. Medlin, K. Hattar, J. A. Zimmerman, F. Abdeljawad, S. M. Foiles, Defect character at grain boundary facet junctions: Analysis of an asymmetric Σ = 5 grain boundary in Fe. Acta Mater. 124, 383–396 (2017).

- J.-P. Couzinié, O. Hardouin Duparc, S. Lartigue-Korinek, J. Thibault-Pénisson, B. Décamps, L. Priester, On the atomic structure of an asymmetrical near Σ = 27 grain boundary in copper. *Philos. Mag. Lett.* 89, 757–767 (2009).
- V. Randle, G. S. Rohrer, H. M. Miller, M. Coleman, G. T. Owen, Five-parameter grain boundary distribution of commercially grain boundary engineered nickel and copper. *Acta Mater.* 56, 2363–2373 (2008).
- N. Thangaraj, U. Dahmen, Grain boundary structure and morphology in 30°<100> tricrystal films of Al. MRS Online Proceedings Library (OPL) 238, 171–176 (1991).
- K. Miyazawa, Y. Iwasaki, K. Ito, Y. Ishida, Combination rule of Σ values at triple junctions in cubic polycrystals. Acta Cryst. 52, 787–796 (1996).
- A. Garg, W. A. T. Clark, J. P. Hirth, Dissociated and faceted large-angle coincident-sitelattice boundaries in silicon. *Philos. Mag. A* 59, 479–499 (1989).
- T. Radetic, F. Lançon, U. Dahmen, Chevron defect at the intersection of grain boundaries with free surfaces in Au. Phys. Rev. Lett. 89, 085502 (2002).
- S. L. Thomas, K. Chen, J. Han, P. K. Purohit, D. J. Srolovitz, Reconciling grain growth and shear-coupled grain boundary migration. *Nat. Commun.* 8, 1764 (2017).
- D. S. Gianola, S. van Petegem, M. Legros, S. Brandstetter, H. van Swygenhoven, K. J. Hemker, Stress-assisted discontinuous grain growth and its effect on the deformation behavior of nanocrystalline aluminum thin films. *Acta Mater.* 54, 2253–2263 (2006).
- S. Plimpton, Fast parallel algorithms for short-range molecular dynamics. J. Comput. Phys. 117, 1–19 (1995).
- G. Grochola, S. P. Russo, I. K. Snook, On fitting a gold embedded atom method potential using the force matching method. J. Chem. Phys. 123, 204719 (2005).
- A. Stukowski, Visualization and analysis of atomistic simulation data with OVITO—The open visualization tool. *Model. Simul. Mat. Sci. Eng.* 18, 015012 (2009).

#### Acknowledgments

**Funding:** G.W. acknowledges support from National Science Foundation (NSF DMR 1808046) through the University of Pittsburgh. C.D. and J.X. acknowledge the use of computing resources provided by WestGrid and Compute/Calcul Canada. **Author contributions:** S.X.M. conceived the project. Z.F. conducted the in situ TEM experiments and performed the experimental data analysis under the direction of S.X.M. S.T. contributed to the TEM observation. J.X. and C.D. carried out MD simulations. All authors contributed to the discussion of the results. Z.F., J.X., C.D., G.W., and S.X.M. wrote the manuscript. **Competing interests:** The authors declare that they have no competing interests. **Data and materials availability:** All data needed to evaluate the conclusions in the paper are present in the paper and/or the Supplementary Materials.

Submitted 22 November 2021 Accepted 27 September 2022 Published 11 November 2022 10.1126/sciadv.abn3785

# **Science** Advances

## Atomic-scale observation of dynamic grain boundary structural transformation during shear-mediated migration

Zhengwu FangJianwei XiaoSusheng TanChuang DengGuofeng WangScott X. Mao

Sci. Adv., 8 (45), eabn3785. • DOI: 10.1126/sciadv.abn3785

View the article online

https://www.science.org/doi/10.1126/sciadv.abn3785 **Permissions** 

https://www.science.org/help/reprints-and-permissions